Viscoelastic flows in mixing-separating cells

A. M. Afonso · M. A. Alves · R. J. Poole ·
P. J. Oliveira · F. T. Pinho

Abstract   The flow of Newtonian and viscoelastic fluids in a mixing-separating geometry that consists of two opposed channel flows interacting through a gap in the common separating wall is investigated. The flow in this type of geometry was studied experimentally by Cochrane et al. (Philos Trans R Soc Lond A301:163–181, 1981) using Newtonian and viscoelastic fluids at low Reynolds numbers (Re < 50). In this numerical study, by use of a finite-volume method, the effects of Deborah (De) and Reynolds numbers and gap size on the two-dimensional flow dynamics are assessed. The normalized gap size varies between 0 and 5, Re varies between 0 and 50 and De varies between 0 and the maximum attainable value. Due to the anti-symmetry of the fully developed inlet conditions and the symmetry of the flow geometry, the Newtonian creeping flow is anti-symmetric. Increasing the gap size of the separating walls leads to an increase of the reversed flow-rate ratio (R_r), which is defined as the ratio of the reversed and the total flow rate. For creeping flow of viscoelastic fluids, here described by the upper-convected Maxwell model, two distinct flow patterns are observed. Below a critical gap size, the reversed flow is slightly enhanced when the Deborah number increases. Further increase of De leads to a subsequent decrease in R_r towards zero. For a supercritical gap size, increasing the Deborah number leads to a monotonic increase in R_r.

Keywords   Elastic instabilities · Flow bifurcation · Mixing-separating ·
Upper-convected Maxwell (UCM) model · Viscoelastic fluids

A. M. Afonso · M. A. Alves
Department of Chemical Engineering, CEFT, Faculty of Engineering, University of Porto, 4200-465 Porto, Portugal

R. J. Poole
Department of Engineering, University of Liverpool, Liverpool L69 3GH, UK

P. J. Oliveira
Department of Electromechanical Engineering, MTP Unit, University of Beira Interior, 6201-001 Covilhã, Portugal

F. T. Pinho (✉)
Department of Mechanical Engineering, CEFT, Faculty of Engineering, University of Porto, 4200-465 Porto, Portugal
e-mail: fpinho@fe.up.pt

1 Introduction

In this work we investigate the flow in a mixing and separating geometry [1] for low-Reynolds-number flow conditions, including the limit of vanishing inertia (creeping flow). The simplest differential constitutive equation describing viscoelastic behaviour, the upper-convected Maxwell (UCM) model, is used in the present numerical study. The flow in this geometry was also investigated experimentally and numerically by Cochrane et al. [1], Walters and Webster [2], Humphrey and Li [3] and Humphrey et al. [4]. Baloch et al. [5] and Fiétier [6] analysed this flow numerically under different conditions.

Cochrane et al. [1] employed a finite-difference method and selected the UCM model to describe the rheological behaviour of a highly elastic constant-viscosity "Boger" fluid [7]. These investigators analysed the effects of gap width (g) using two different flow configurations: (i) matching flow rates in the two inlet channel arms and (ii) unbalanced inlet flow rates. In a follow-up work [2], thin insert plates with rounded edges were used. For both experimental studies it was found that the flow displayed distinctive Newtonian and viscoelastic behaviours, with the occurrence of unidirectional and reversed flows in varying extents. Later, Baloch et al. [5] selected the simplified Phan-Thien–Tanner (sPTT) model [8] to describe the rheological behaviour, and simulated this flow also using thin insert plates with rounded edges, for the case of equal flow rates at the inlet channels (the sPTT model is a simplified version of the Phan-Thien–Tanner model that does not account for the slip between the molecular network and the continuum medium, i.e., the PTT model with $\xi = 0$). Fiétier [6] simulated the flow of a FENE-P model [9] using a spectral-element method, and considered the case with a thick insert plate with rounded edges. The numerical results obtained captured qualitatively the experimental results presented by Walters and Webster [2]. Humphrey and Li [3] used a dye visualization technique, which revealed the time-evolution of pairs of transversely aligned vortices in a confined counter-current shearing flow configuration, for moderate Reynolds numbers (Re = 100–1000). More recently, Humphrey et al. [4] simulated the time-dependent flow of a Newtonian fluid in a counter-current shearing flow configuration, for $100 < \text{Re} < 300$.

In the present numerical investigation we present a detailed analysis of the viscoelastic fluid-flow behaviour in the mixing and separating geometry, mapping different steady flow behaviours as a function of gap size under conditions of low inertia and different elasticity levels. The occurrence and extent of purely elastic flow instabilities leading to a bifurcation of steady flows is also assessed. These instabilities usually arise in extensionally dominated flows with strong streamline curvature, such as flows with a stagnation point (e.g. cross-slot flow [10–12], or the opposed jet apparatus [13]). In their numerical investigation, Poole et al. [11] studied the two-dimensional cross-slot flow of an UCM fluid for creeping and low-Re-flow conditions, and reproduced qualitatively the occurrence of a steady bi-stable asymmetric flow, above a critical Deborah number. Further increase of De led to a second transition to a time-dependent flow as observed in the experimental work of Arratia et al. [10]. Later, Poole et al. [12] included the effects of solvent viscosity and finite extensibility (using the Oldroyd-B and sPTT models), and delimited different flow patterns in β-Re-De and ε-Re-De maps. These flow maps showed the existence of a narrow region of steady asymmetric flow in the β-ε-Re-De parameter space and identified the critical De for occurrence of time-dependent flow.

Elastic instabilities are not restricted to extensional flows and are found in shear flows, as widely documented by Morozov and van Saarloos [14]. Earlier investigations on elastic instabilities in Poiseuille and Couette flows were reported by Ho and Denn [15] and Joo and Shaqfeh [16], and criteria for their onset were proposed by Shaqfeh [17] and McKinley et al. [18].

In this investigation we focus on the mixing-separating flow geometry with thin insert plates and equal flow rates at the two channel inlets under low-Re flow conditions. Newtonian and viscoelastic fluids, described using the UCM model, are used. This flow combines, under certain conditions, regions of extensional flows with shear flows, but shear effects play an important role under all conditions.

The remainder of this paper is organised as follows: initially the governing equations are presented, followed by a brief description of the finite-volume method used in the simulations. Afterwards, we describe the flow geometry and the computational meshes used before presenting the numerical results obtained. The paper ends with the main conclusions.

2 Governing equations and numerical method

The equations we need to solve are those of conservation of mass and momentum of an incompressible fluid,

$$\nabla \cdot \mathbf{u} = 0, \tag{1}$$

$$\rho \frac{\partial \mathbf{u}}{\partial t} + \rho \nabla \cdot \mathbf{uu} = -\nabla p + \nabla \cdot \boldsymbol{\tau}, \tag{2}$$

coupled with a constitutive equation for the extra-stress tensor, $\boldsymbol{\tau}$. For reasons of rheological simplicity, we use the UCM model which is described by the evolution equation

$$\boldsymbol{\tau} + \lambda \left(\frac{\partial \boldsymbol{\tau}}{\partial t} + \mathbf{u} \cdot \nabla \boldsymbol{\tau} \right) = \eta \left(\nabla \mathbf{u} + \nabla \mathbf{u}^{\mathrm{T}} \right) + \lambda \left(\boldsymbol{\tau} \cdot \nabla \mathbf{u} + \nabla \mathbf{u}^{\mathrm{T}} \cdot \boldsymbol{\tau} \right), \tag{3}$$

where λ and η are the relaxation time and shear viscosity of the fluid, respectively.

A fully implicit finite-volume method was used to solve (1)–(3). The method is based on a time-marching pressure-correction algorithm formulated with the collocated variable arrangement, as described in detail in previous works [19,20]. Recently, this numerical method was adapted to use the *log-conformation* methodology proposed by Fattal and Kupferman [21], and this technique is used here because of the enhanced numerical stability. The main modifications implicated in the use of the log-conformation method are described in detail by Afonso et al. [22], which is why they are not repeated here. In summary, the governing equations are initially transformed to a non-orthogonal coordinate system, but the dependent variables are kept in a Cartesian coordinate system. Afterwards, the equations are integrated in space over the control volumes of the computational mesh, and in time over a small time step (δt), leading to sets of linearised algebraic equations of the general form:

$$a_{\mathrm{P}} u_{i,\mathrm{P}} = \sum_{\mathrm{F}=1}^{6} a_{\mathrm{F}} u_{i,\mathrm{F}} + S_{u_i}, \tag{4}$$

to be solved for the velocity components, and

$$a_{\mathrm{P}}^{\Theta} \Theta_{ij,\mathrm{P}} = \sum_{\mathrm{F}=1}^{6} a_{\mathrm{F}}^{\Theta} \Theta_{ij,\mathrm{F}} + S_{\Theta_{ij}} \tag{5}$$

to be solved for the logarithm of the conformation tensor, Θ_{ij}. In Eqs. 4 and 5 a_{F} represents coefficients accounting for advection and diffusion (only advection in Eq. 5) and S contains the source terms with all contributions that are not included in the terms with coefficients. The subscript P denotes a generic cell and subscript F the corresponding neighbour cells. The central coefficient of the momentum equation, a_{P}, is given by

$$a_{\mathrm{P}} = \frac{\rho V_{\mathrm{P}}}{\delta t} + \sum_{\mathrm{F}=1}^{6} a_{\mathrm{F}}. \tag{6}$$

The sets of linear equations (4) are solved sequentially for the Cartesian velocity components. This newly computed velocity field usually does not satisfy the continuity equation and needs to be adjusted by an adequate correction of the pressure field that drives it. This adjustment is accomplished through a pressure-correction field determined from a Poisson pressure equation, following the ideas of the SIMPLEC algorithm [23]. Once a velocity field that satisfies the continuity equation has been obtained, the implicitly discretized constitutive equations (i.e., Eq. 5) are solved sequentially. To formulate the advective fluxes of the constitutive equation, we use the CUBISTA high-resolution scheme, a third-order method specifically designed for differential rheological constitutive equations [20]. In this work we will focus primarily on creeping-flow conditions, in which case the advective term of the momentum equation (i.e., the left side of (2)) is neglected. When inertial flows are considered, we include the advective term of the momentum equation, and also use the CUBISTA high-resolution scheme in the evaluation of the advective fluxes.

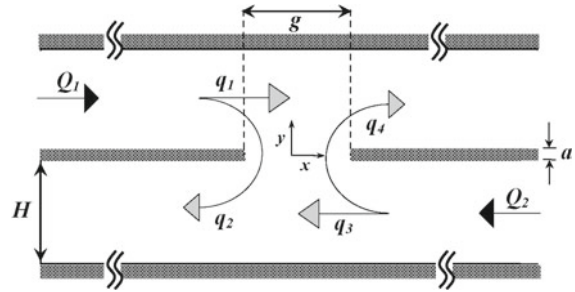**Fig. 1** Schematic diagram of the mixing-and-separating flow geometry

Table 1 Main characteristics of the computational meshes ($\theta = 1$)

	NC	DOF	NCS_X	NCS_Y	$\Delta x_{min}/H$	$\Delta y_{min}/H$
M25 ($\theta = 1$)	6,300	37,800	26	25	0.0385	0.04
M51 ($\theta = 1$)	25,704	154,224	52	51	0.0186	0.0196
M101 ($\theta = 1$)	102,212	613,272	104	101	0.0093	0.0099

3 Flow geometry and computational meshes

The flow under investigation is that of two opposed channels interacting through a gap of nondimensional width $\theta = g/H$, in the middle of a thin separating wall of nondimensional thickness $\alpha = a/H$, as illustrated in Fig. 1. The two inlet and outlet channels have the same width (H) and lengths $L = 20H$.

Fully developed velocity and stress profiles are imposed at the two inlets. Preliminary studies confirmed that the inlet and outlet channel lengths are sufficiently long to avoid interference of the inlet and/or outflow boundary conditions upon the flow in the central region. At all channel walls, no-slip boundary conditions are imposed. At the outlet planes Neumann boundary conditions ($\partial \varphi / \partial x = 0$) are applied to all variables including the pressure gradient.

For all gap values analysed the computational domain was mapped using six orthogonal blocks, one in each of the four channels and two blocks in the central region. The main characteristics of the three consecutively refined meshes used in this work are presented in Table 1, for the case with $\theta = 1$. Table 1 includes information regarding the total number of cells of the meshes (NC), the number of control volumes in the central region in both x- and y-directions (NCS), and the minimum cell spacing (Δx_{min} and Δy_{min}), which also occurs in the central region. For other plate thicknesses and gap values, the meshes were adapted in order to have the same minimum cell spacing at the central region of the meshes. For each value of θ investigated, different meshes were generated with different number of cells in the x- and y-directions, but always ensuring consistent mesh refinement and that the minimum cell spacing in both directions remained essentially the same (i.e., square control volumes in the region of interest). Consequently, in all meshes the central region of the mesh is uniform, and progressively refined from $\Delta x_{min}/H = \Delta y_{min}/H \approx 0.04$ to 0.02 and 0.01 for meshes M25, M51 and M101, respectively. These two-dimensional meshes contain 102,212 and 122,816 cells (M101) corresponding to 613,272 and 736,896 degrees-of-freedom (DOF), for low and large nondimensional gap widths, respectively.

The results discussed in the next section are presented in dimensionless form, unless otherwise stated. Velocities are normalised using the bulk velocity in the inlet channels (U) and the extra-stresses are normalised using a characteristic viscous stress, $\eta U/H$. The Deborah number represents the ratio between the relaxation time of the fluid (λ) and a characteristic time scale of the flow, here chosen as g/U. Consequently, in the present investigation we define the Deborah number as $De = \lambda U/g$.

For flows with non-negligible inertia the Reynolds number is also important, and is here defined as $Re = \rho U H/\eta$. The degree of flow reversal relative to the unidirectional flow that would exist in the absence of a gap in the middle wall is quantified using the parameter $R_r = q_2/Q_1 = q_4/Q_2$, where q_2 and q_4 correspond to the partial flow rates
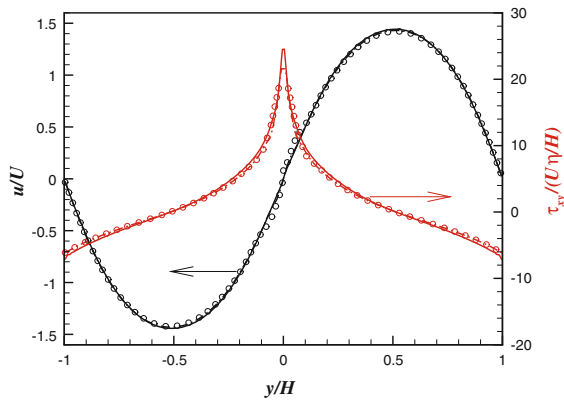
Fig. 2 Transverse profiles of the normalised velocity and shear stress at $x/H = 0$, for De = 0.35 (Re = 0, $\theta = \sqrt{2}$ and $\alpha \to 0$), on mesh M25 (*open circle*), mesh M51 (*dashed line*) and mesh M101 (*full line*)
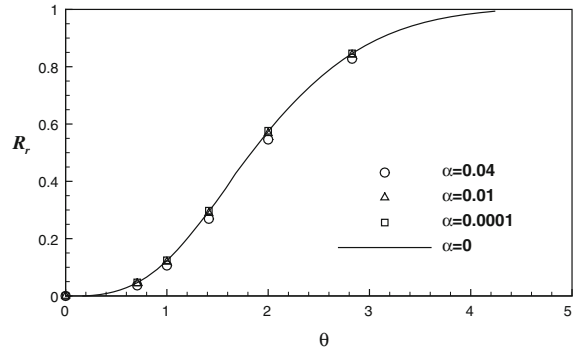

Fig. 3 Degree of reverse flow as function of gap width, θ, and plate thickness, α, for the Newtonian case at Re = 0

Table 2 Quantification of numerical uncertainty for some representative cases: Couette correction

De	θ	C_{corr}				Error (%)		
		M25	M51	M101	Extr.	M25	M51	M101
0.42	1.414	1.496	1.486	1.482	1.480	1.069	0.369	0.127
0.26	1.74	2.348	2.194	2.180	2.179	7.768	0.674	0.0585
0.3	2.0	2.475	2.396	2.378	2.373	4.303	0.980	0.223

Errors relative to the extrapolated solution

per unit depth that reverse from each inlet arm and $Q_1 = Q_2 = UH$ are the total flow rates per unit depth at each inlet channel, as shown in Fig. 1.

4 Results and discussion

4.1 Assessment of numerical accuracy

In this section we estimate the numerical uncertainty analysing the convergence with mesh refinement. In Fig. 2 we plot the transverse profiles of the dimensionless velocity and shear stress along the vertical line ($x = 0$) that crosses the stagnation point located at the middle of the gap. The data from all the meshes correspond to the creeping flow of an UCM fluid at De = 0.35, for a dimensionless gap $\theta = \sqrt{2}$ and for a separating wall with negligible thickness ($\alpha = 0$). The velocity profiles calculated in meshes M51 and M101 exhibit excellent agreement. The stress profiles show a slight mesh dependency near the stagnation point, due to the high stress gradients that occur in that region, but elsewhere the agreement between all meshes is very good.

Additional information on the accuracy of the numerical results is presented in Table 2, where the estimated error for the Couette correction (C_{corr}) coefficient (discussed in Sect. 4.4 and defined in Eq. 7) is provided for all three meshes and for three different nondimensional gap widths ($\theta = \sqrt{2}$, 1.74 and 2) for a range of Deborah numbers. The uncertainties were estimated by comparison with the C_{corr} extrapolated using Richardson's extrapolation technique [24]. As can be observed, the uncertainties estimated for meshes M51 and M101 are always below 1%, showing again the high level of accuracy of the numerical results. Therefore, in the remainder of the paper, unless otherwise stated, the results presented were obtained with the intermediate mesh M51.
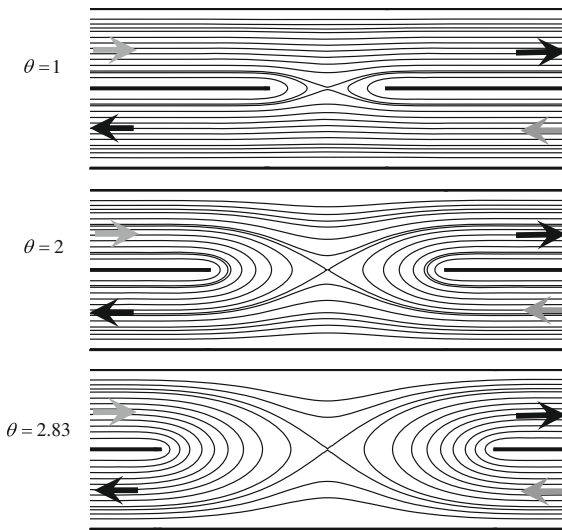
Fig. 4 Streamlines for the mixing-and-separating geometry for several gap widths, θ, with $\alpha = 0$, for the Newtonian case at Re $= 0$
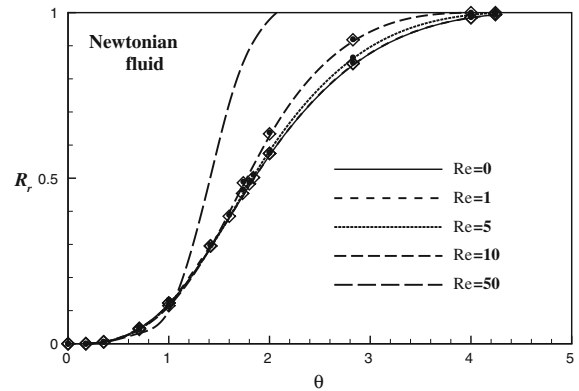

Fig. 5 Degree of reverse flow as function of gap width, θ, for several Reynolds numbers. Newtonian case on meshes M25 (*diamond*), M51 (*lines*) and M101 (*closed circle*)

4.2 Newtonian fluid flow

Geometrically, the mixing-and-separating geometry can be idealized as a cross-slot device [10] with one pair of aligned arms rotated by 90° towards the other pair, leading to a nondimensional gap size of $\theta = \sqrt{2}$ and a vanishing thickness of the separation plate ($\alpha \rightarrow 0$). If during this transformation the flow type would not change, the ratio between the reversed to unidirectional flow would be $R_r = 0.5$, in order to keep full similarity with the cross-slot. Obviously, this is not the case as illustrated in Fig. 3, where R_r is plotted as a function of normalized gap width, θ, for various plate thicknesses, α, for creeping flow of a Newtonian fluid. For this shear dominated flow we obtain $R_r = 0.29$ for $\theta = \sqrt{2}$. In order to achieve $R_r = 0.5$, the normalized gap should be about $\theta \approx 1.75$. From Fig. 3 we conclude that the effect of plate thickness for thin plates is small in agreement with experiments [1,2]. Figure 3 also highlights that the transition from a straight unperturbed no-reverse-flow situation at low θ to a full flow reversal occurs when the dimensionless gap size becomes large.

The differences between the results for the cross-slot and the mixing-and-separating geometries can be explained from the different angles of the approaching flows in the vicinity of the stagnation points. In the mixing-and-separating geometry these approach flows are not aligned with the channels and are not orthogonal as occurs in the cross-slot flow. Consequently, in the mixing-and-separating geometry the shear flow is important in the stagnation point region, being absent in the cross-slot flow geometry which is purely extensional in character, except in the vicinity of the channel walls. This difference may also be important for understanding the onset of purely elastic instabilities in the cross-slot geometry [14,25]. These observations are better understood when analysing the streamline plots presented in Fig. 4, which correspond to creeping flow of Newtonian fluids at low, medium and large dimensionless gap widths ($\theta = 1$, 2 and 2.83). These patterns correspond to the $\alpha = 0$ curve represented in Fig. 3, where the corresponding reversed flow rate ratios take the numerical values of 0.123, 0.575 and 0.846, i.e., increasing with gap size.

Figure 5 illustrates the influence of flow inertia on R_r for Newtonian fluids as a function of the dimensionless gap width, θ. For all Reynolds numbers analysed, R_r varies from 0 to 1 as the gap sizes increases in agreement with experiments [1,2]. For conditions of low inertia (say, Re $\leq$ 1) the variation of R_r with θ is independent of Reynolds number. However, when inertial effects are significant, flow reversal is enhanced. In Fig. 5 we plot data
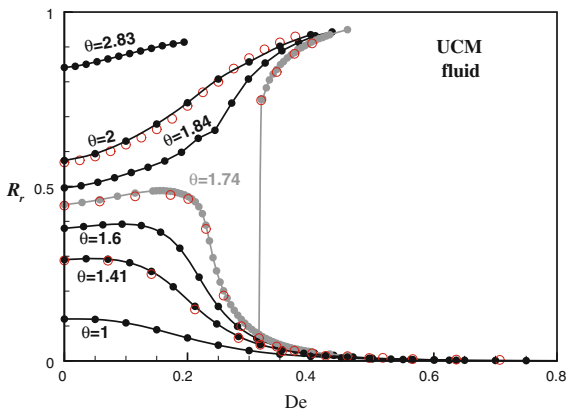
Fig. 6 Degree of reverse flow as function of Deborah number for several gap widths, θ, and Re $= 0$ (*closed symbols*—Mesh M51 and *open symbols*—Mesh M101)
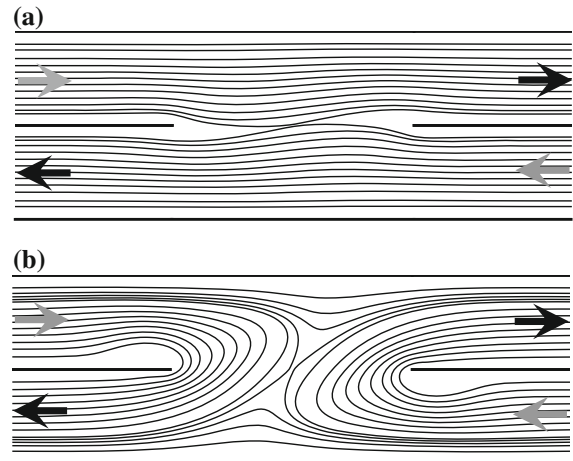

Fig. 7 Streamlines for $\theta = 1.74$, $\alpha = 0$, Re $= 0$ and De $= 0.345$ in mesh M101: the two bifurcated solutions have **a** $R_r = 0.041$ and **b** $R_r = 0.83$

of R_r at some representative Reynolds numbers as function of θ for each of the three meshes, and once again, mesh dependency is barely noticeable.

4.3 Viscoelastic and inertial effects

Figure 6 illustrates an interesting bifurcation which depends on the gap width and occurs with UCM fluids under creeping flow conditions. For large dimensionless gap sizes, but below a critical value ($\theta \leq 1.6$), the reversed flow is slightly enhanced initially as viscoelasticity increases, followed by a significant decrease towards zero when De further increases. This behaviour is characterized by a significant departure from streamline parallelism in the gap region, although with the fluid still tending to flow unidirectionally in agreement with experiments [1,2]. This situation is illustrated by the flow pattern of Fig. 7a.

In contrast, for a supercritical dimensionless gap size ($\theta \geq 1.84$) we find that viscoelasticity is now responsible for a continuous increase of R_r with De, and the corresponding flow patterns are similar to those illustrated in Fig. 7b. It is important to emphasize that this supercritical pattern has not yet been observed experimentally primarily due to the stabilising effect of inertia, to be discussed below.

For creeping flow and at a definite intermediate gap width range ($1.6 \leq \theta \leq 1.84$, cf. Fig. 6 for $\theta = 1.74$) a steady bifurcation flow pattern emerges, with a sudden jump between two widely different flow configurations, ranging from almost unidirectional to almost fully reversed, at Deborah numbers slightly higher than the critical Deborah number. The corresponding streamline plots are illustrated in Fig. 7 for De $= 0.345$ and $\theta = 1.74$. On the upper plot the flow is almost unidirectional ($R_r = 0.047$) while at the bottom plot the flow is highly reversed ($R_r = 0.85$). The bifurcation between these two flow patterns is due to a purely elastic instability since inertia has no role (Re $= 0$) in the present simulations (we have also observed such purely elastic instabilities in the references [11,12,26]). Incidentally, when $\theta = 1.74$ we find a maximum value of $R_r = 0.5$ before bifurcation (at De ≈ 0.2) and this corresponds to the situation where the approach flows at the stagnation point tend to become closer to perpendicular. Here, we found that the critical Deborah number for the onset of the bifurcation of UCM fluids is De$_{crit} = 0.316$, a similar value to that reported for the instability in the cross-slot geometry (De$_{crit} \approx 0.31$ [11], with this De defined as θDe). The predictions also indicated that in this intermediate region of bifurcated flow the critical De decreases in inverse proportion to θ.

Most of these simulations, as well as those with inertia to be discussed, started from a quiescent flow field (with all components of the velocity vector and the stress tensor set to zero). For the critical gap size, beyond which the
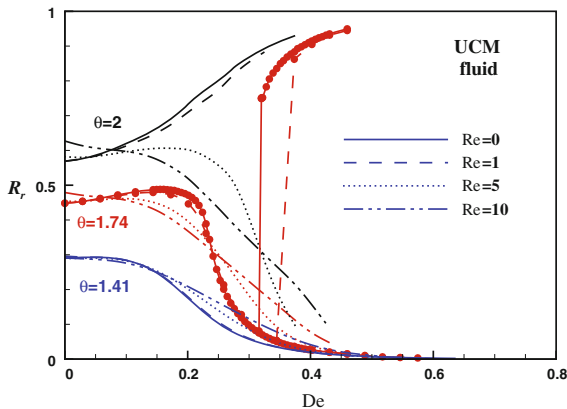
Fig. 8 Degree of reverse flow as function of Deborah number for several gap widths, θ, and Re = 0, 1, 5 and 10
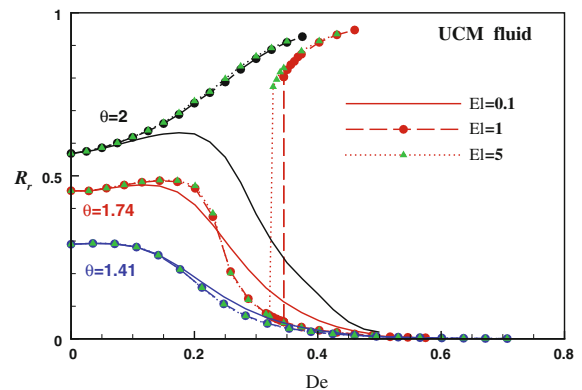
Fig. 9 Degree of reverse flow as function of Deborah number for several gap widths, θ, and elasticity numbers (El = 0.1, 1 and 5)

flow bifurcated to the two steady and opposite solutions, most of the simulations converged to the lower branch. In a few cases (at the higher De values) the solution evolved to the upper branch of the bifurcation. To be able to capture the upper branch in a wide range of De, De was decreased in small steps starting from a computed solution (at the upper branch) as initial guess. However, as the critical De is approached the numerical solution quickly changes to the lower branch, even when varying De in very small steps.

Regarding the influence of flow inertia, the critical De for the steady bifurcation is found to increase with Re, as illustrated in Fig. 8 for $\theta = 1.74$ and Re = 1. Here, R_r is plotted as a function of De for three different dimensionless gap widths ($\theta = \sqrt{2}$, 1.74 and 2) and for Re up to 10. As observed for the Newtonian fluids, the degree of flow reversal is essentially independent of Reynolds number for Re $\leq$ 1. At higher Reynolds numbers (e.g. Re = 5 and 10) and $\theta = 2$ we observe an inversion in the flow configurations: whereas at low Re viscoelasticity was seen to be responsible for an increase in R_r (the typical supercritical behaviour), at large Reynolds numbers R_r decreases with De (the typical subcritical behaviour). Thus, strong inertial effects eliminate the elastic bifurcation and the flow becomes more unidirectional. This behaviour is also in contrast with the Newtonian case where for the same value of $\theta = 2$ an increase in the Reynolds number increased the reversed flow. This opposed effect of flow inertia at low and high elasticity explains why the supercritical behaviour has not yet been observed in experiments and suggests the need for further experimental work, using a highly viscous and elastic fluid, to attain low Reynolds numbers flow at high Deborah numbers. An interesting alternative is to use microfluidic geometries, in which the small sizes lead to a decrease of flow inertia and to a significant enhancement of viscoelasticity (note that De increases when the length scale decreases) [27].

In order to clarify the trends in Fig. 8 and mimic the procedure of experiments, we conducted an additional set of simulations with constant elasticity number (El = De/Re = $\lambda \eta / \rho H^2 \theta$), a situation that better reproduces the experimental scenario, where an increase of the flow rate leads to a proportional increase of Re and De, without altering the elasticity number (which is independent of flow rate). Using such an approach, the combined effects of elasticity and inertia are quantified by the elasticity number, and these effects are presented in Fig. 9, where R_r is plotted as a function of De for three different gap widths ($\theta = \sqrt{2}$, 1.74 and 2) and for three different values of El (El = 0.1, 1 and 5). For a subcritical gap size ($\theta = \sqrt{2}$) the effect of El is small, with the reversed flow slightly attenuated by viscoelasticity, followed by a strong decrease in R_r towards zero as De further increases. For the intermediate gap width ($\theta = 1.74$), the steady bifurcation flow patterns are not observed for low elasticity numbers (El = 0.1), and the critical Deborah number increases as El decreases, showing the stabilising effect of inertia. Finally, for a supercritical gap size ($\theta = 2$) we can observe again an inversion in the flow configurations for low El, with R_r decreasing with De, thus the flow becomes more unidirectional.

4.4 Steady bifurcation flow stability

As discussed in the previous sections, for intermediate gap widths ($1.6 \leq \theta \leq 1.84$) a steady bifurcation flow pattern is observed. For Deborah numbers higher than a critical value, two different steady flow patterns with different flow configurations can be observed. In order to assess the stability of these dual configurations we performed a simple test for $\theta = 1.74$, the results of which are shown in Fig. 10. Time-dependent flow simulations were performed for a periodic variation of Deborah number, departing from a De near the critical value (De = 0.322, corresponding to a highly reversed configuration flow, $R_r = 0.75$), down to De = 0.316 (corresponding to a quasi unidirectional configuration flow, $R_r = 0.076$), using a second-order time discretization scheme [28] with a small time step ($\Delta t/\lambda = 2 \times 10^{-5}$), for good accuracy in time. After one cycle of De, the flow configuration shifts from a reversed to a unidirectional configuration, remaining in this configuration along the rest of the pulsating variation. This observation suggests that the unidirectional configuration is preferred. An alternative explanation to this behaviour is based on the energy losses of the two flow configurations, here quantified using a Couette correction coefficient (C_{corr}), evaluated as the normalized pressure drop between inlet and outlet after discounting for the fully developed pressure drop along the channels (i.e., C_{corr} represents a dimensionless extra pressure drop):

$$C_{\text{corr}} = \frac{\Delta p - \Delta p_{FD}}{2\tau_w}, \tag{7}$$

where Δp is the pressure difference between any of the inlets and one of the outlets, Δp_{FD} is the pressure drop required to drive fully developed flow in the inlet and outflow straight channels, as in the absence of the interference of the gap, and τ_w is the wall shear stress under fully developed conditions (given by $\tau_w = 6\eta U/H$ for the UCM model). The value of C_{corr} for Newtonian fluids as a function of the non-dimensional gap size is presented in Fig. 11a, showing that C_{corr} increases asymptotically to about 1.3 as θ increases beyond 2, corresponding to increased levels of reversed flow. So, extrapolating these findings to the viscoelastic case, we conclude that the preferred configuration (unidirectional flow) corresponds to the less dissipative flow field, a situation that has been reported in other similar instabilities in cross slot and flow focusing geometries [11,26,29]. This difference is also clear in the results for C_{corr} obtained for an intermediate gap width ($\theta = 1.74$) and plotted as a function of De in Fig. 11b. The reversed flow is initially slightly enhanced up to De = 0.25 (recall Fig. 6) and mainly because strong hoop stresses are established due to fluid elasticity and flow curvature, the value of C_{corr} increases significantly above the Newtonian level, and this is followed by a decrease of the Couette correction when the flow starts to become more unidirectional as De is further increased. At Deborah numbers above the De$_{\text{crit}}$, and for the reversed configuration flow, it is clear that the energy losses are significantly higher than for the corresponding unidirectional flow configuration, correlating with the results presented in Fig. 10.

5 Conclusions

The UCM model has been used to simulate viscoelastic fluid flows in a mixing-separating geometry [1]. For a combination of critical flow parameters, it was possible to identify a new steady bi-stable bifurcation in the flow patterns at low inertia and high elasticity.

Under creeping-flow conditions the UCM model exhibited two distinct flow patterns. For normalized gap sizes below a critical value, the reversed flow is slightly enhanced as De increases, followed by a strong decrease towards zero of the reversed flow rate as De further increases. In contrast, above a supercritical gap size increasing De leads to a monotonic increase in R_r. For near-critical flow geometries it was possible to observe a sudden transition between the two flow conditions at slightly different Deborah numbers. Flow inertia was found to increase the critical Deborah number for steady flow bifurcation. Inertia naturally enhances the straight flow configuration and at Re = 5, R_r always decreased with Deborah number for De ≤ 0.6 and for the investigated gap sizes. The interplay between inertia and elastic effects is clarified using the elasticity number, El, instead of Re and De separately. Essentially the viscoelastic fluid adjusts itself so as to avoid changes in the flow direction and when the streamline curvature imposed by the geometry (increasing θ) is large, the elastic normal stresses become so strong, with consequent high
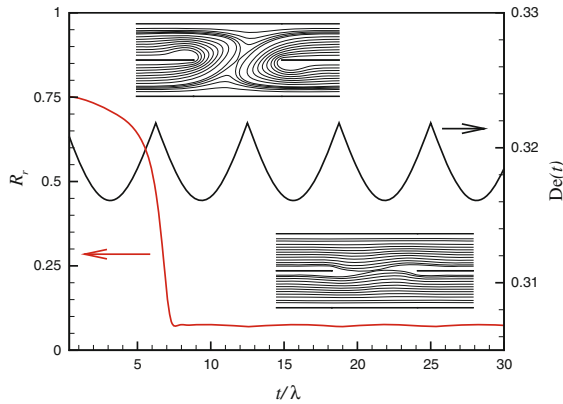
Fig. 10 Stability analysis for $\theta = 1.74$, with $\alpha = 0$, Re $= 0$ and De $= [0.316, 0.322]$
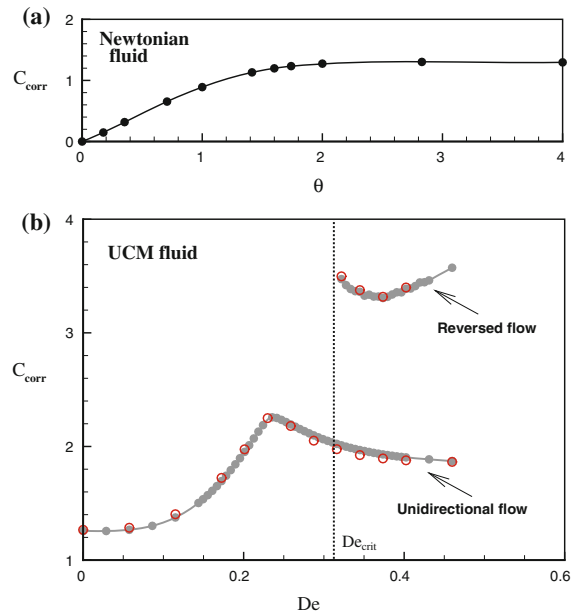
Fig. 11 Couette correction coefficient under creeping flow conditions and zero thickness (Re $= 0$ and $\alpha = 0$) as function of: **a** dimensionless gap size, θ, in Newtonian flow (De $= 0$); **b** Deborah numbers for UCM fluid flow ($\theta = 1.74$). (*closed circle* Mesh M51; *open circle* M101)

energy loss coefficient, that the reversed flow pattern can no longer be sustained. There is then a sudden jump from reversed flow (large curvature) to unidirectional flow (small curvature), accompanied by a reduction of the energy loss associated with the flow. In addition, for a limited range of flow parameters, a pair of extreme flow patterns might co-exist as a solution of the governing equation, as an indication of a steady bifurcation phenomenon.

These results suggest the need for experiments with highly viscous and elastic fluids (or at microscale where Re is naturally reduced and De is enhanced) in order to identify the supercritical behaviour, which has so far not been reported in the literature.

References

1. Cochrane T, Walters K, Webster MF (1981) On Newtonian and non-Newtonian flow in complex geometries. Philos Trans R Soc Lond A301:163–181
2. Walters K, Webster MF (1982) On dominating elasto-viscous response in some complex flows. Philos Trans R Soc Lond A308: 199–218
3. Humphrey JAC, Li SK-K (1981) Tilting, stretching, pairing and collapse of vortex structures in confined counter-current flow. J Fluids Eng 103:466–470
4. Humphrey JAC, Rosales JL, Legendre LA, LeDuc JP, Landers JP (2008) Vortex dynamics in confined counter-current shearing flows with applications to mixing. Int J Heat Fluid Flow 29:1089–1102
5. Baloch A, Townsend P, Webster MF (1995) On the simulation of highly elastic complex flows. J Non-Newton Fluid Mech 59: 111–128
6. Fiétier N (2002) Numerical simulations of viscoelastic fluid flows by spectral element methods and time-dependent algorithm. PhD thesis, EPFL, Lausanne

7. Boger DV (1977) Highly elastic constant-viscosity fluid. J Non-Newton Fluid Mech 3:87–91
8. Phan-Thien N, Tanner RI (1977) New constitutive equation derived from network theory. J Non-Newton Fluid Mech 2:353–365
9. Bird RB, Dotson PJ, Johnson NL (1980) Polymer solution rheology based on a finitely extensible bead-spring chain model. J Non-Newton Fluid Mech 7:213–235
10. Arratia PE, Thomas CC, Diorio JD, Gollub JP (2006) Elastic instabilities of polymer solutions in cross-channel flow. Phys Rev Lett 96:144502
11. Poole RJ, Alves MA, Oliveira PJ (2007) Purely elastic flow asymmetries. Phys Rev Lett 99:164503
12. Poole RJ, Alves MA, Afonso A, Pinho FT, Oliveira PJ (2007) Purely elastic instabilities in a cross-slot flow. In: The SoR 79th annual meeting, Salt Lake City, USA
13. Chow A, Keller A, Müller AJ, Odell JA (1988) Entanglements in polymer solutions under elongational flow: a combined study of chain stretching, flow velocimetry and elongational viscosity. Macromolecules 21:250–256
14. Morozov AN, van Saarloos W (2007) An introductory essay on subcritical instabilities and the transition to turbulence in viscoelastic parallel shear flows. Phys Rep 447:112–143
15. Ho TC, Denn MM (1978) Stability of plane Poiseulle flow of a highly elastic liquid. J Non-Newton Fluid Mech 3:179–195
16. Joo YL, Shaqfeh ESG (1992) A purely elastic instability in Dean and Taylor–Dean flow. Phys Fluids A 4:527–543
17. Shaqfeh ESG (1996) Purely elastic instabilities in viscometric flows. Annu Rev Fluid Mech 28:129–185
18. McKinley GH, Pakdel P, Oztekin A (1996) Rheological and geometric scaling of purely elastic flow instabilities. J Non-Newton Fluid Mech 67:19–46
19. Oliveira PJ, Pinho FT, Pinto GA (1998) Numerical simulation of non-linear elastic flows with a general collocated finite-volume method. J Non-Newton Fluid Mech 79:1–43
20. Alves MA, Oliveira PJ, Pinho FT (2003) A convergent and universally bounded interpolation scheme for the treatment of advection. Int J Numer Methods Fluids 41:47–75
21. Fattal R, Kupferman R (2004) Constitutive laws of the matrix-logarithm of the conformation tensor. J Non-Newton Fluid Mech 123:281–285
22. Afonso A, Oliveira PJ, Pinho FT, Alves MA (2009) The log-conformation tensor approach in the finite-volume method framework. J Non-Newton Fluid Mech 157:55–65
23. van Doormal JP, Raithby GD (1984) Enhancements of the SIMPLE method for predicting incompressible fluid flows. Numer Heat Transf 7:147–163
24. Ferziger JH (1981) Numerical methods for engineering applications. Wiley, New York
25. Afonso AM, Alves MA, Pinho FT (2010) Purely-elastic instabilities in three-dimensional cross slot geometries. J Non-Newton Fluid Mech 165:743–751
26. Rocha GN, Poole RJ, Alves MA, Oliveira PJ (2009) On extensibility effects in the cross-slot flow bifurcation. J Non-Newton Fluid Mech 156:58–69
27. Stone HA, Stroock AD, Ajdari A (2004) Engineering flows in small devices: microfluidics toward a Lab-on-a-Chip. Annu Rev Fluid Mech 36:381–411
28. Oliveira PJ (2001) Method for time-dependent simulations of viscoelastic flows: vortex shedding behind cylinder. J Non-Newton Fluid Mech 101:113–137
29. Oliveira MSN, Pinho FT, Poole RJ, Oliveira PJ, Alves MA (2009) Purely-elastic flow asymmetries in flow-focusing devices. J Non-Newton Fluid Mech 160:31–39